Advances in Nano Research, *Vol. 19, No. 3 (2025) 273-284*
https://doi.org/10.12989/anr.2025.19.3.273

Physics-informed deep neural networks for sports applications: Enhancing tennis handle performance with nanocomposites

Ying Ying Tao[1], Liquan Chen*[2] and Murat Yaylaci[3,4]

[1]*Department of Physical Education, Communication University of Zhejiang, Hangzhou, Zhejiang, 310000, China*
[2]*School of Culture and Tourism, Quzhou College of Technology, Quzhou, Zhejiang, 324000, China*
[3]*Department of Civil Engineering, Recep Tayyip Erdogan University, 53100, Rize, Turkey*
[4]*Turgut Kıran Maritime Faculty, Recep Tayyip Erdogan University, 53900, Rize, Turkey*

(*Received April 22, 2024, Revised September 2, 2025, Accepted September 3, 2025*)

Abstract. In this paper, we propose a new framework that merges physics-informed deep neural networks (PINNs) with novel material modeling to assess the performance of tennis handles reinforced with graphene oxide powder nanocomposites. The tennis handle is modeled as a thin shell structure within the cylindrical coordinate framework to accurately capture the complex curved geometry of the handle as well as its vibration response under dynamic loading conditions. The effective mechanical properties of the nanocomposite reinforced structure use the Halpin–Tsai micromechanical model to represent the ability of the graphene oxide powders to reinforce the polymeric matrix. The structural response is captured in terms of a higher-order shear deformation theory (HSDT) based on Taylor's series expansion, which is an improvement compared to classical and conventional first-order shear models typically used due to its ability to account for variation in shear strain through thickness. The governing motion equations are developed through Hamilton's principle, accounting for both inertial and elastic energy contributors. To tackle the resulting high-dimensional system, a PINN architecture with Legendre polynomial expansions provides a physics-constrained and computationally efficient surrogate representation for detailed vibration and stability analyses. Legendre polynomials allow the neural network to have a larger representation capacity while grasping smoothness and orthogonality within the solution space. Results show that the stiffness, damping, and energy absorption capacity of tennis handles improved significantly with graphene oxide nanocomposites. Also, the proposed PINN framework achieved better accuracy than traditional numerical methods, such as finite differences, computer finite element analysis, calculations made using Matlab simulation toolboxes, and higher-order polynomial interpolation. This hybrid physics–AI methodology improves sports by assisting with the optimization of tennis handle designs and also provides a generalized method for the use of physics-informed machine learning in sports equipment design.

Keywords: Hamilton's principle; higher-order shear deformation theory; graphene oxide powder nanocomposites; physics-informed deep neural networks; sports engineering

1. Introduction

Composite and nanocomposite reinforced structures have gained tremendous importance in modern engineering due to their superior mechanical, thermal, and functional properties compared to conventional materials (Azmi *et al*. 2019). They combine two or more distinct phases to produce a material with enhanced performance that cannot be achieved by individual constituents alone (Ebrahimi, Dehghan *et al*. 2019a). In aerospace engineering, composite structures are widely used because of their high strength-to-weight ratio, which reduces fuel consumption and improves efficiency (Ebrahimi *et al*. 2019b). Automotive industries employ composites to manufacture lightweight yet durable components, thereby enhancing vehicle performance and reducing emissions (Hajmohammad *et al*. 2018a). Marine applications benefit from composites due to their excellent corrosion resistance and fatigue durability under harsh environments (Jayakumari *et al*. 2024). Civil engineering incorporates composites in bridges, buildings, and rehabilitation projects where long-term durability is critical (Madenci *et al*. 2023). Medical implants and devices rely on biocompatible composites for their strength, stability, and adaptability within biological environments (Moradi *et al*. 2022). In renewable energy, composite blades in wind turbines significantly improve energy capture efficiency while resisting environmental degradation (Xia *et al*. 2023). Sports equipment like bicycles, tennis rackets, and helmets leverage composites for better performance and safety (Ye *et al*. 2024). Beyond traditional composites, nanocomposite reinforced structures introduce nanoscale fillers, such as carbon nanotubes, graphene, and nanoclays, into polymer, ceramic, or metal matrices (Zerrouki *et al*. 2020). These nanofillers dramatically improve stiffness, toughness, and fracture resistance due to their high aspect ratio and extraordinary intrinsic properties (Zhao *et al*. 2022). Nanocomposites also enhance thermal conductivity and electrical performance, enabling multifunctional applications (Liu *et al*. 2021). In electronics, polymer nanocomposites with conductive nanoparticles are used to fabricate flexible and lightweight devices (Bentrar *et al*. 2023, Beitollahi *et*

*Corresponding author, Ph.D.,
E-mail: 18105706608@163.com

ISSN: 2287-237X (Print), 2287-2388 (Online)

al. 2025). Packaging industries utilize nanocomposites for improved barrier properties against gases and moisture, extending product shelf life (Gawah *et al*. 2025). Biomedical fields integrate nanocomposites into scaffolds, drug delivery systems, and tissue engineering for superior bioactivity (Gawah *et al*. 2024). Defense and military applications rely on nanocomposite armor and coatings to achieve high strength and lightweight protection (Youzera *et al*. 2025). The aerospace sector increasingly adopts nanocomposite-reinforced polymers for damage tolerance and vibration damping (Al-Houri *et al*. 2024). Nanocomposites are also significant in energy storage systems, such as lithium-ion batteries and supercapacitors, due to their enhanced electrochemical stability (Tounsi *et al*. 2024). Environmental engineering benefits from nanocomposite membranes for advanced water purification and gas separation. Sustainability goals are addressed through nanocomposites by enabling greener materials with lower energy demands and longer life cycles (Belabed 2024). One of the major advantages of nanocomposites is their tunability, allowing designers to optimize properties by varying filler type, dispersion, and alignment (Belabed *et al*. 2024). They provide opportunities for smart and adaptive materials capable of sensing, actuating, and self-healing under operational conditions (Avcar *et al*. 2023). Compared with traditional reinforcements, nanocomposites can achieve superior properties with very low filler content (Djebbour *et al*. 2025). The interdisciplinary nature of nanocomposite research bridges materials science, physics, chemistry, and engineering (Ebrahimi and Salari 2018). Rapid advances in nanotechnology continue to expand the potential applications of nanocomposite reinforced structures (Ehyaei *et al*. 2016). Despite challenges in large-scale manufacturing and cost, their advantages in performance make them highly attractive for future industries (Kadiri *et al*. 2024). Ongoing research focuses on improving dispersion techniques and interfacial bonding to fully exploit nanofillers' potential (Hajmohammad *et al*. 2018b). As global demands for stronger, lighter, and more sustainable materials increase, composites and nanocomposites will remain at the forefront of innovation (Salari *et al*. 2019). Their ability to address mechanical, thermal, electrical, and environmental challenges positions them as transformative materials across multiple sectors (Shen *et al*. 2024). Therefore, composite and nanocomposite reinforced structures represent a crucial pathway toward high-performance, multifunctional, and sustainable engineering solutions (Safarpour *et al*. 2021). A schematic view of the tennis Handle as a sports equipment that is similar to a cylindrical shell in a real application with a circular cross-section of the handle is shown in Fig. 1.

The present research explores the integration of physics-informed deep neural networks with advanced composite modeling to enhance the structural and functional performance of tennis handles reinforced with graphene oxide powder nanocomposites. The handle is idealized as a cylindrical shell structure, providing a robust framework for analyzing its vibrational and mechanical responses under realistic playing conditions. The Halpin–Tsai micromechanical model is employed to determine the effective elastic properties of the graphene oxide–polymer composite, capturing nanoscale reinforcement effects. To account for transverse shear

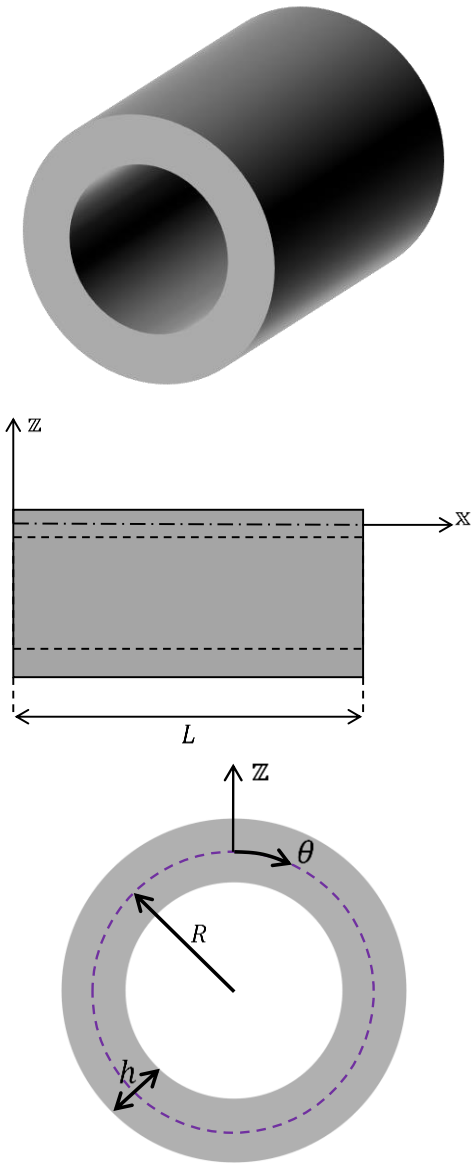

Fig. 2 Diagrammatic depiction of a composite shell

deformations and higher-order kinematic fields, the structural formulation adopts a Taylor's series expansion-based higher-order shear deformation theory. The governing equations of motion are systematically derived through Hamilton's principle, ensuring consistency in energy-based modeling of dynamic behavior. For solution and predictive modeling, a deep neural network framework embedded with Legendre polynomial expansions is proposed, serving as a physics-informed surrogate capable of resolving complex boundary-value problems. The Legendre expansion enriches the approximation capability of the network, promoting stability and convergence in capturing displacement, stress, and vibration fields. Numerical investigations reveal that graphene oxide powder reinforcement leads to substantial gains in stiffness-to-weight ratio, damping efficiency, and vibration suppression of tennis handles. Furthermore, the PINN-based approach demonstrates high accuracy with reduced computational cost when benchmarked against conventional finite element methods. The study provides

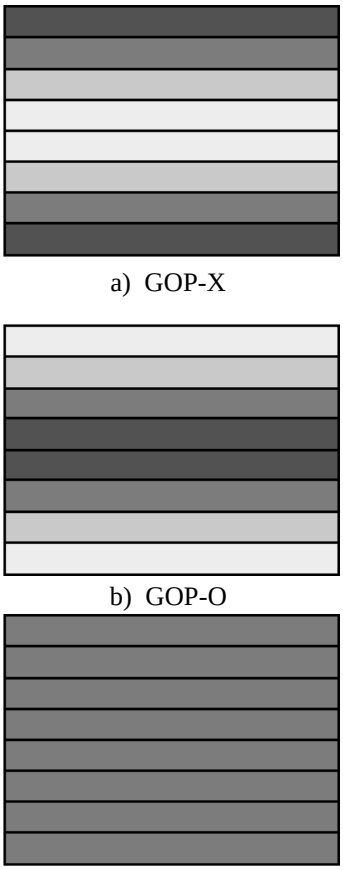

a) GOP-X

b) GOP-O

c) GOP-UD

Fig. 3 GOP distribution patterns in the thickness of the system

new insights into the synergistic use of nanocomposite materials and AI-driven solvers for advancing sports engineering applications, particularly in optimizing tennis handle design for improved durability and player performance.

2. Theory and formulation

Examine a shell as seen in Fig. 2. To get the wave motion equations, one must assume the cylindrical coordinate system $(\mathbb{x}, \theta, \mathbb{z})$.

There are two methods to give reinforcements, or GOPs: globally (GOP-UD) or functionally graded using GOP-X and GOP-O, two distinct patterns. The figures are shown in Fig. 3.

2.1 Properties of composite media

The GOP reinforced composite cylindrical shells feature three different patterns in terms of material properties that change with thickness: GOP-UD, where GOP is evenly distributed throughout the thickness; GOP-X, where the concentration of GOP rises from the center to the surfaces; and GOP-O, where the concentration of GOP rises from the surfaces to the center (Fig. 3). Consequently, the material properties of a concrete shell reinforced with GOP may be obtained using the data presented in Ref. (Vu and Tran 2025). The Poisson's ratio (ν_{GOPRC}), density (ρ_{GOPRC}), Young's modulus (E_{GOPRC}), and thermal expansion coefficient (α_{GOPRC}) are some of these variables. The Halpin-Tsai model is used to estimate these attributes.

$$\begin{aligned} \rho_{GOPRC} &= \rho_{GOP}V_{GOP} + \rho_m V_m, \\ \nu_{GOPRC} &= \nu_{GOP}V_{GOP} + \nu_m V_m, \\ E_{GOPRC} &= 0.49E_l + 0.51E_t, \\ \alpha_{GOPRC} &= \alpha_m + \frac{\alpha_m + \alpha_{GOP}}{1/K_m + 1/K_{GOP}}\left(\frac{1}{K_{eff}} + \frac{1}{K_m}\right). \end{aligned} \tag{1}$$

The matrix density (m) and reinforcement (GOP) are denoted by the symbols ρ_m and ρ_{GOP}, respectively. The volume fractions of the reinforcement and matrix are denoted by the variables V_m, and V_{GOP}, respectively. The reinforcement and matrix the symbols for Poisson's ratios are ν_m and ν_{GOP}, respectively. The longitudinal and transverse moduli of the cylindrical shell of the GOP-reinforced nanocomposite are denoted by the symbols E_l and E_t, respectively. K is the bulk modulus, while α is the thermal expansion coefficient. Based on the different patterns, the volume percentage of GOP (V_{GOP}) in different layers is calculated.

$$\begin{aligned} GOP - X{:}\, V_{GOP} &= 4\left|\frac{\mathbb{z}}{h}\right| V'_{GOP}, \\ GOP - \mathrm{O}{:}\, V_{GOP} &= 2\left(1 - 2\left|\frac{\mathbb{z}}{h}\right|\right) V'_{GOP}, \\ GOP - \mathrm{UD}{:}\, V_{GOP} &= V'_{GOP}. \end{aligned} \tag{2}$$

The volume fraction of GOPs (V_{GOP})) and the volume fraction of the matrix (V_m) have the following relationship:

$$V_{GOP} + V_m = 1 \tag{3}$$

According to Eq. (2), V'_{GOP} is the volume fraction that represents the cumulative GOP percentage within the rotating shell.

$$V'_{GOP} = \frac{W_{GOP}}{W_{GOP} + (1 - W_{GOP})(\rho_{GOP}/\rho_m)} \tag{4}$$

The GOP's weighted percentage is shown by W_{GOP}. The longitudinal modulus (E_l) and transverse modulus (E_t) values are given by Eq. (1).

$$E_l = \frac{1 + \xi_l \eta_l V_{GOP}}{1 - \eta_l V_{GOP}} \times E_m, \; E_t = \frac{1 + \xi_t \eta_t V_{GOP}}{1 - \eta_t V_{GOP}} \times E_m \tag{5}$$

The parameters in this case are η_t and η_l, and the matrix material's Young's moduli, denoted by E_m, are as follows:

$$\eta_l = \frac{\frac{E_{GOP}}{E_m} - 1}{\frac{E_{GOP}}{E_m} + \xi_l}, \eta_t = \frac{\frac{E_{GOP}}{E_m} - 1}{\frac{E_{GOP}}{E_m} + \xi_t} \tag{6}$$

When the geometry components ξ_l and ξ_t are specified as:

$$\xi_l = \xi_t = \frac{2d_{GOP}}{h_{GOP}} \tag{7}$$

where the diameter (d_{GOP}) and thickness (h_{GOP}) of GOP are shown.

2.2 Displacement field

The following set of equations is obtained by formulating a 3-D elasticity problem using the Taylor's series expansion and expanding the displacement components $\mathfrak{A}(\mathbb{x},\theta,\mathbb{z},t)$, $\mathfrak{B}(\mathbb{x},\theta,\mathbb{z},t)$, and $\mathfrak{C}(\mathbb{x},\theta,\mathbb{z},t)$ of any point in the shell space in terms of the thickness coordinate $\mathbb{z}$ (Garg *et al*. 2006).

$$\mathfrak{A}(\mathbb{x},\theta,\mathbb{z},t)=\mathfrak{A}_0(\mathbb{x},\theta,t)+\mathbb{z}\mathfrak{A}_1(\mathbb{x},\theta,t)+\mathbb{z}^2\mathfrak{A}_2(\mathbb{x},\theta,t)+\mathbb{z}^3\mathfrak{A}_3(\mathbb{x},\theta,t), \tag{8a}$$

$$\mathfrak{B}(\mathbb{x},\theta,\mathbb{z},t)=\mathfrak{B}_0(\mathbb{x},\theta,t)+\mathbb{z}\mathfrak{B}_1(\mathbb{x},\theta,t)+\mathbb{z}^2\mathfrak{B}_2(\mathbb{x},\theta,t)+\mathbb{z}^3\mathfrak{B}_3(\mathbb{x},\theta,t), \tag{8b}$$

$$\mathfrak{C}(\mathbb{x},\theta,\mathbb{z},t)=\mathfrak{C}_0(\mathbb{x},\theta,t)+\mathbb{z}\mathfrak{C}_1(\mathbb{x},\theta,t)+\mathbb{z}^2\mathfrak{C}_2(\mathbb{x},\theta,t)+\mathbb{z}^3\mathfrak{C}_3(\mathbb{x},\theta,t), \tag{8c}$$

Moreover, the strain tensor components could be obtained from as below (Sadd, 2009):

$$\begin{aligned}&\mathcal{E}_{\mathbb{x}\mathbb{x}}=\frac{\partial\mathfrak{A}}{\partial\mathbb{x}},\ \mathcal{E}_{\theta\theta}=\frac{1}{R}\left(\frac{\partial\mathfrak{B}}{\partial\theta}+\mathfrak{C}\right),\\ &\mathcal{E}_{\mathbb{z}\mathbb{z}}=\frac{\partial\mathfrak{C}}{\partial\mathbb{z}},\ \mathfrak{f}_{\theta\mathbb{z}}=\frac{\partial\mathfrak{B}}{\partial\mathbb{z}}+\frac{1}{R}\frac{\partial\mathfrak{C}}{\partial\theta}-\frac{\mathfrak{B}}{R},\\ &\mathfrak{f}_{\mathbb{x}\mathbb{z}}=\frac{\partial\mathfrak{C}}{\partial\mathbb{x}}+\frac{\partial\mathfrak{A}}{\partial\mathbb{z}},\ \mathfrak{f}_{\mathbb{x}\theta}=\frac{1}{r}\frac{\partial\mathfrak{A}}{\partial\theta}+\frac{\partial\mathfrak{B}}{\partial\mathbb{x}}.\end{aligned} \tag{9}$$

Relation between stress and strain components as follows:

$$\sigma_{\mathbb{x}\mathbb{x}}=\mathcal{T}_{11}\mathcal{E}_{\mathbb{x}\mathbb{x}}+\mathcal{T}_{12}\mathcal{E}_{\theta\theta}+\mathcal{T}_{13}\mathcal{E}_{\mathbb{z}\mathbb{z}}, \tag{10a}$$

$$\sigma_{\theta\theta}=\mathcal{T}_{12}\mathcal{E}_{\mathbb{x}\mathbb{x}}+\mathcal{T}_{22}\mathcal{E}_{\theta\theta}+\mathcal{T}_{23}\mathcal{E}_{\mathbb{z}\mathbb{z}}, \tag{10b}$$

$$\sigma_{\mathbb{z}\mathbb{z}}=\mathcal{T}_{13}\mathcal{E}_{\mathbb{x}\mathbb{x}}+\mathcal{T}_{23}\mathcal{E}_{\theta\theta}+\mathcal{T}_{33}\mathcal{E}_{\mathbb{z}\mathbb{z}}, \tag{10c}$$

$$\sigma_{\theta\mathbb{z}}=\mathcal{T}_{44}\mathfrak{f}_{\theta\mathbb{z}}, \tag{10d}$$

$$\sigma_{\mathbb{x}\mathbb{z}}=\mathcal{T}_{55}\mathfrak{f}_{\mathbb{x}\mathbb{z}}, \tag{10e}$$

$$\sigma_{\mathbb{x}\theta}=\mathcal{T}_{66}\mathfrak{f}_{\mathbb{x}\theta}. \tag{10f}$$

where

$$\begin{aligned}&\mathcal{T}_{11}=\frac{E_{GOPRC}(1-\nu_{GOPRC})}{(1+\nu_{GOPRC})(1-2\nu_{GOPRC})},\mathcal{T}_{33}=\mathcal{T}_{22}=\mathcal{T}_{11},\\ &\mathcal{T}_{12}=\frac{E_{GOPRC}\nu_{GOPRC}}{(1+\nu_{GOPRC})(1-2\nu_{GOPRC})},\mathcal{T}_{13}=\mathcal{T}_{23}=\mathcal{T}_{12},\\ &\mathcal{T}_{44}=\frac{E_{GOPRC}}{2(1+\nu_{GOPRC})},\mathcal{T}_{66}=\mathcal{T}_{55}=\mathcal{T}_{44}.\end{aligned} \tag{11}$$

2.3 Hamilton's principle and governing equations

Hamilton's principle is used to derive the governing equations of motion:

$$\delta\int_{t_1}^{t_2}(T-U-W)\,dt=0 \tag{12}$$

where U is strain energy; T is kinetic energy; W work done by thermal load.

The kinetic energy of the functionally graded cylindrical shells may be reformulated as follows.

$$\mathrm{T}=\frac{1}{2}\int_0^L\int_0^{2\pi}\int_{-h/2}^{h/2}\rho(\mathbb{z})[\dot{\mathfrak{A}}^2+(\dot{\mathfrak{B}})^2+(\dot{\mathfrak{C}})^2]R\,d\mathbb{z}\,d\theta\,d\mathbb{x}, \tag{13}$$

The functionally graded cylindrical shells' strain energy is provided as follows:

$$\mathrm{U}=\frac{1}{2}\int_A\int_{-h/2}^{h/2}(\sigma_{\mathbb{x}\mathbb{x}}\mathcal{E}_{\mathbb{x}\mathbb{x}}+\sigma_{\theta\theta}\mathcal{E}_{\theta\theta}+\sigma_{\mathbb{z}\mathbb{z}}\mathcal{E}_{\mathbb{z}\mathbb{z}}+\sigma_{\mathbb{x}\theta}\mathfrak{f}_{\mathbb{x}\theta}+\sigma_{\theta\mathbb{z}}\mathfrak{f}_{\theta\mathbb{z}}+\sigma_{\mathbb{x}\mathbb{z}}\mathfrak{f}_{\mathbb{x}\mathbb{z}})dA \tag{14}$$

Afterward, the variation of the work induced by thermal gradient is formulated as

$$W=\frac{1}{2}\int_A n^T(\nabla^2\mathfrak{C})\mathfrak{C}\,dA \tag{15}$$

Force resultant of thermal loading n^T involved in Eq. (15) can be determined by the following relation

2.4 Machine learning

Another critical component to achieve acoustically adjustable headphones (in real-time) made of smart nanomaterials is machine learning. Training models with large datasets of movie audio tracks makes the system learn about the various scene types: dialogue-intensive sequences, action sequences or music sequences. The acoustic needs in each category are different - say, making speech more intelligible in dialogues, enhancing low-frequency action effects, or reduce tonal coloration of musical scenes. When trained, the model accepts the incoming stream of audio in real time, identifies the scene and produces control parameters directing the nanomaterial diaphragm to respond in a manner that best optimizes sound transfer.

When machine learning is coupled with nanomaterial-based hardware, it creates a self-driven (feedback) system which is dynamically adjusted to content and environment. Environmental sensors, such as microphones to measure ambient noise, add even more data to the model to allow the algorithm to adapt its choices in changing circumstances. This ensures the sound quality is unchanged regardless of whether you are in a very quiet room or a crowded social place. The headphones, ability to ensure such an immersive and highly customized movie experience with regards to intelligent classification and the extremely high capability of a nanomaterial to create an amazingly rich acoustic perspective that a traditional audio system could never. The basic relation for this method is:

$$y(t)=f_\theta(x(t),e(t)) \tag{43}$$

where $y(t)$ denotes the output control, $x(t)$ is the input parameter, $e(t)$ shows the environmental context and f_θ indicates the trained machine learning model.

$$n^T=\int_{-h/2}^{h/2}(\mathcal{T}_{11}+\mathcal{T}_{12}+\mathcal{T}_{13})\alpha_{GOPRC}\Delta T\,d\mathbb{z} \tag{16}$$

In addition, substituting Eqs. (13)-0(15) into Eq. (12), results in the following equations for each degree of freedom:

$$\delta\mathfrak{A}_0\colon \frac{\partial n_{\mathbb{x}\mathbb{x}}}{\partial \mathbb{x}}+\frac{1}{R}\frac{\partial n_{\mathbb{x}\theta}}{\partial \theta}=\mathfrak{F}_0\ddot{\mathfrak{A}}_0+\mathfrak{F}_1\ddot{\mathfrak{A}}_1+\mathfrak{F}_2\ddot{\mathfrak{A}}_2+\mathfrak{F}_3\ddot{\mathfrak{A}}_3, \quad (17a)$$

$$\delta\mathfrak{B}_0\colon \frac{1}{R}\frac{\partial n_{\theta\theta}}{\partial \theta}+\frac{\partial n_{\mathbb{x}\theta}}{\partial \mathbb{x}}+\frac{n_{\theta\mathbb{z}}}{R}=\mathfrak{F}_0\ddot{\mathfrak{B}}_0+\mathfrak{F}_1\ddot{\mathfrak{B}}_1+\mathfrak{F}_2\ddot{\mathfrak{B}}_2+\mathfrak{F}_3\ddot{\mathfrak{B}}_3, \quad (17b)$$

$$\delta\mathfrak{C}_0\colon \frac{1}{R}\frac{\partial n_{\theta\mathbb{z}}}{\partial \theta}+\frac{\partial n_{\mathbb{x}\mathbb{z}}}{\partial \mathbb{x}}-\frac{n_{\theta\theta}}{R}-n^T\nabla^2\mathfrak{C}=\mathfrak{F}_0\ddot{\mathfrak{C}}_0+\mathfrak{F}_1\ddot{\mathfrak{C}}_1+\mathfrak{F}_2\ddot{\mathfrak{C}}_2+\mathfrak{F}_3\ddot{\mathfrak{C}}_3, \quad (17c)$$

$$\delta\mathfrak{A}_1\colon \frac{\partial m_{\mathbb{x}\mathbb{x}}}{\partial \mathbb{x}}+\frac{1}{R}\frac{\partial m_{\mathbb{x}\theta}}{\partial \theta}-n_{\mathbb{x}\mathbb{z}}=\mathfrak{F}_1\ddot{\mathfrak{A}}_0+\mathfrak{F}_2\ddot{\mathfrak{A}}_1+\mathfrak{F}_3\ddot{\mathfrak{A}}_2+\mathfrak{F}_4\ddot{\mathfrak{A}}_3, \quad (17d)$$

$$\delta\mathfrak{B}_1\colon \frac{1}{R}\frac{\partial m_{\theta\theta}}{\partial \theta}+\frac{\partial m_{\mathbb{x}\theta}}{\partial \mathbb{x}}+\frac{m_{\theta\mathbb{z}}}{R}-n_{\theta\mathbb{z}}=\mathfrak{F}_1\ddot{\mathfrak{B}}_0+\mathfrak{F}_2\ddot{\mathfrak{B}}_1+\mathfrak{F}_3\ddot{\mathfrak{B}}_2+\mathfrak{F}_4\ddot{\mathfrak{B}}_3, \quad (17e)$$

$$\delta\mathfrak{C}_1\colon \frac{1}{R}\frac{\partial m_{\theta\mathbb{z}}}{\partial \theta}+\frac{\partial m_{\mathbb{x}\mathbb{z}}}{\partial \mathbb{x}}-\frac{m_{\theta\theta}}{R}-n_{\mathbb{z}\mathbb{z}}-n^T\left(\frac{h}{2}\right)\nabla^2\mathfrak{C}=\mathfrak{F}_1\ddot{\mathfrak{C}}_0+\mathfrak{F}_2\ddot{\mathfrak{C}}_1+\mathfrak{F}_3\ddot{\mathfrak{C}}_2+\mathfrak{F}_4\ddot{\mathfrak{C}}_3, \quad (17f)$$

$$\delta\mathfrak{A}_2\colon \frac{\partial p_{\mathbb{x}\mathbb{x}}}{\partial \mathbb{x}}+\frac{1}{R}\frac{\partial p_{\mathbb{x}\theta}}{\partial \theta}-m_{\mathbb{x}\mathbb{z}}=\mathfrak{F}_2\ddot{\mathfrak{A}}_0+\mathfrak{F}_3\ddot{\mathfrak{A}}_1+\mathfrak{F}_4\ddot{\mathfrak{A}}_2+\mathfrak{F}_5\ddot{\mathfrak{A}}_3, \quad (17g)$$

$$\delta\mathfrak{B}_2\colon \frac{1}{R}\frac{\partial p_{\theta\theta}}{\partial \theta}+\frac{\partial p_{\mathbb{x}\theta}}{\partial \mathbb{x}}+\frac{p_{\theta\mathbb{z}}}{R}-m_{\theta\mathbb{z}}=\mathfrak{F}_2\ddot{\mathfrak{B}}_0+\mathfrak{F}_3\ddot{\mathfrak{B}}_1+\mathfrak{F}_4\ddot{\mathfrak{B}}_2+\mathfrak{F}_5\ddot{\mathfrak{B}}_3, \quad (17h)$$

$$\delta\mathfrak{C}_2\colon \frac{1}{R}\frac{\partial p_{\theta\mathbb{z}}}{\partial \theta}+\frac{\partial p_{\mathbb{x}\mathbb{z}}}{\partial \mathbb{x}}-\frac{p_{\theta\theta}}{R}-m_{\mathbb{z}\mathbb{z}}-n^T\left(\frac{h}{2}\right)^2\nabla^2\mathfrak{C}=\mathfrak{F}_2\ddot{\mathfrak{C}}_0+\mathfrak{F}_3\ddot{\mathfrak{C}}_1+\mathfrak{F}_4\ddot{\mathfrak{C}}_2+\mathfrak{F}_5\ddot{\mathfrak{C}}_3, \quad (17i)$$

$$\delta\mathfrak{A}_3\colon \frac{\partial q_{\mathbb{x}\mathbb{x}}}{\partial \mathbb{x}}+\frac{1}{R}\frac{\partial q_{\mathbb{x}\theta}}{\partial \theta}-p_{\mathbb{x}\mathbb{z}}=\mathfrak{F}_3\ddot{\mathfrak{A}}_0+\mathfrak{F}_4\ddot{\mathfrak{A}}_1+\mathfrak{F}_5\ddot{\mathfrak{A}}_2+\mathfrak{F}_6\ddot{\mathfrak{A}}_3, \quad (17j)$$

$$\delta\mathfrak{B}_3\colon \frac{1}{R}\frac{\partial q_{\theta\theta}}{\partial \theta}+\frac{\partial q_{\mathbb{x}\theta}}{\partial \mathbb{x}}+\frac{q_{\theta\mathbb{z}}}{R}-p_{\theta\mathbb{z}}=\mathfrak{F}_3\ddot{\mathfrak{B}}_0+\mathfrak{F}_4\ddot{\mathfrak{B}}_1+\mathfrak{F}_5\ddot{\mathfrak{B}}_2+\mathfrak{F}_6\ddot{\mathfrak{B}}_3, \quad (17k)$$

$$\delta\mathfrak{C}_3\colon \frac{1}{R}\frac{\partial q_{\theta\mathbb{z}}}{\partial \theta}+\frac{\partial q_{\mathbb{x}\mathbb{z}}}{\partial \mathbb{x}}-\frac{q_{\theta\theta}}{R}-p_{\mathbb{z}\mathbb{z}}-n^T\left(\frac{h}{2}\right)^3\nabla^2\mathfrak{C}=\mathfrak{F}_3\ddot{\mathfrak{C}}_0+\mathfrak{F}_4\ddot{\mathfrak{C}}_1+\mathfrak{F}_5\ddot{\mathfrak{C}}_2+\mathfrak{F}_6\ddot{\mathfrak{C}}_3. \quad (17l)$$

where

$$\begin{Bmatrix} n_{\mathbb{x}\mathbb{x}} \\ n_{\theta\theta} \\ n_{\mathbb{z}\mathbb{z}} \end{Bmatrix}=\int_{\forall}\left(\begin{Bmatrix} \sigma_{\mathbb{x}\mathbb{x}} \\ \sigma_{\theta\theta} \\ \sigma_{\mathbb{z}\mathbb{z}} \end{Bmatrix}\right)d\forall,$$

$$\begin{Bmatrix} m_{\mathbb{x}\mathbb{x}} \\ m_{\theta\theta} \\ m_{\mathbb{z}\mathbb{z}} \end{Bmatrix}=\int_{\forall}\left(\mathbb{z}\times\begin{Bmatrix} \sigma_{\mathbb{x}\mathbb{x}} \\ \sigma_{\theta\theta} \\ \sigma_{\mathbb{z}\mathbb{z}} \end{Bmatrix}\right)d\forall,$$

$$\begin{Bmatrix} p_{\mathbb{x}\mathbb{x}} \\ p_{\theta\theta} \\ p_{\mathbb{z}\mathbb{z}} \end{Bmatrix}=\int_{\forall}\left(\mathbb{z}^2\times\begin{Bmatrix} \sigma_{\mathbb{x}\mathbb{x}} \\ \sigma_{\theta\theta} \\ \sigma_{\mathbb{z}\mathbb{z}} \end{Bmatrix}\right)d\forall, \quad (18)$$

$$\begin{Bmatrix} q_{\mathbb{x}\mathbb{x}} \\ q_{\theta\theta} \\ q_{\mathbb{z}\mathbb{z}} \end{Bmatrix}=\int_{\forall}\left(\mathbb{z}^3\times\begin{Bmatrix} \sigma_{\mathbb{x}\mathbb{x}} \\ \sigma_{\theta\theta} \\ \sigma_{\mathbb{z}\mathbb{z}} \end{Bmatrix}\right)d\forall,$$

$$\begin{Bmatrix} n_{\theta\mathbb{z}} \\ n_{\mathbb{x}\mathbb{z}} \\ n_{\mathbb{x}\theta} \end{Bmatrix}=\int_{\forall}\left(\begin{Bmatrix} \sigma_{\theta\mathbb{z}} \\ \sigma_{\mathbb{x}\mathbb{z}} \\ \sigma_{\mathbb{x}\theta} \end{Bmatrix}\right)d\forall,$$

$$\begin{Bmatrix} m_{\theta\mathbb{z}} \\ m_{\mathbb{x}\mathbb{z}} \\ m_{\mathbb{x}\theta} \end{Bmatrix}=\int_{\forall}\left(\mathbb{z}\begin{Bmatrix} \sigma_{\theta\mathbb{z}} \\ \sigma_{\mathbb{x}\mathbb{z}} \\ \sigma_{\mathbb{x}\theta} \end{Bmatrix}\right)d\forall,$$

$$\begin{Bmatrix} p_{\theta\mathbb{z}} \\ p_{\mathbb{x}\mathbb{z}} \\ p_{\mathbb{x}\theta} \end{Bmatrix}=\int_{\forall}\left(\mathbb{z}^2\begin{Bmatrix} \sigma_{\theta\mathbb{z}} \\ \sigma_{\mathbb{x}\mathbb{z}} \\ \sigma_{\mathbb{x}\theta} \end{Bmatrix}\right)d\forall,$$

$$\begin{Bmatrix} q_{\theta\mathbb{z}} \\ q_{\mathbb{x}\mathbb{z}} \\ q_{\mathbb{x}\theta} \end{Bmatrix}=\int_{\forall}\left(\mathbb{z}^3\begin{Bmatrix} \sigma_{\theta\mathbb{z}} \\ \sigma_{\mathbb{x}\mathbb{z}} \\ \sigma_{\mathbb{x}\theta} \end{Bmatrix}\right)d\forall,$$

$$\{\mathfrak{F}_0,\mathfrak{F}_1,\mathfrak{F}_2,\mathfrak{F}_3,\mathfrak{F}_4,\mathfrak{F}_5,\mathfrak{F}_6\}=\int_{\forall}(\{1,\mathbb{z},\mathbb{z}^2,\mathbb{z}^3,\mathbb{z}^4,\mathbb{z}^5,\mathbb{z}^6\}\rho_{GOPRC})d\forall.$$

3. PINNs solution procedure

Physical laws, expressed as partial differential equations (PDEs), are directly included in neural network training using a deep learning architecture known as Physics-Informed Neural Networks. Instead of relying just on data, PINNs use automated differentiation to apply governing equations, boundary conditions, and beginning conditions as soft constraints in the loss function. Unlike conventional numerical techniques like the finite element method, PINNs do not need a grid, making them mesh-free and very practical for complicated geometries. By integrating the physics into the neural network, PINNs provide a comprehensive solution for both learning unknown parameters and solving nonlinear, coupled electromechanical systems. Because they can also deal with inverse issues and parameter identification, they are an effective technique for scientific computing and engineering applications. When solving governing equations using the PINN technique, the following stages are taken into account:

3.1 Replace legendre polynomial expansions with neural networks (NNs)

Instead of using Legendre polynomial expansions (Eqs. 19a–19d) to estimate the displacement and electric potential fields, we use deep neural networks:

$$\mathfrak{A}_i(\mathbb{x},\theta,t)=N_{\mathfrak{A}_i}(\mathbb{x},\theta,t,\mathbb{T}), \quad (19a)$$

$$\mathfrak{B}_i(\mathbb{x},\theta,t)=N_{\mathfrak{B}_i}(\mathbb{x},\theta,t,\mathbb{T}), \quad (19b)$$

$$\mathfrak{C}_i(\mathbb{x},\theta,t)=N_{\mathfrak{C}_i}(\mathbb{x},\theta,t,\mathbb{T}), \quad (19c)$$

$$i=0,1,2,3. \quad (19d)$$

where $\mathbb{T}$ represents the trainable weights and biases of the neural networks. Each N represents a deep neural network with inputs $(\mathbb{x},\theta,t)$.

3.2 Boundary and initial conditions

Boundary and initial conditions are used to illustrate the loss function:

- Clamped BCs:

$$L_{BC}=\sum\left|\left|\mathfrak{A}_0(\partial\Omega,t)\right|\right|^2+\left|\left|\nabla\mathfrak{A}_0(\partial\Omega,t)\right|\right|^2+\ldots.. \quad (20)$$

- Initial Conditions:

Table 1 The natural frequency (in Hz) of a simply-supported FGM cylindrical shell is compared for various gradient indices (N) and mode numbers (n) when m=1

	$N = 0.5$		$N = 1$		$N = 30$	
n	Present	Loy *et al.* (1999)	Present	Loy *et al.* (1999)	Present	Loy *et al.* (1999)
1	13.335	13.321	13.234	13.211	12.940	12.914
2	4.5286	4.5168	4.477	4.480	4.3805	4.3765
3	4.1823	4.1911	4.1453	4.1569	4.0463	4.0576
4	7.0910	7.0972	7.0320	7.0384	6.8554	6.8726
5	11.322	11.336	11.224	11.241	10.942	10.978

$$L_{IC} = \sum |\mathfrak{A}_0(\mathbb{x},\theta,0) - \mathfrak{A}_0^{data}||^2 + ||\dot{\mathfrak{A}}_0(\mathbb{x},\theta,0) - \dot{\mathfrak{A}}_0^{data}||^2 + \dots \quad (21)$$

3.3 Governing PDE residuals

The mechanical PDEs are imposed as residuals:

- Mechanical Residual: $R_m = m\,\ddot{u} + C\,\dot{u} + Ku - f$

Total PDE loss: $L_{PDE} = \sum ||R_m||^2$

3.4 Damping and stiffness modifications

Including Rayleigh damping and adjusted stiffness:

- Damping Term:

$C = \alpha R_m + \beta R_k u + G_v\left[k_{\psi u}\right]_a\left[k_{\psi\psi}^{-1}\right]_s\left[k_{\psi u}\right]_s$

- Stiffness Term: $K = k_{uu} + G_d[k_{\psi u}]_a[k_{\psi\psi}^{-1}]_s[k_{\psi u}]_s$

3.5 Training loss function

The total loss function:

$$L_{total} = \lambda_{PDE}L_{PDE} + \lambda_{BC}L_{BC} + \lambda_{IC}L_{IC} + \lambda_{\psi_s}L_{\psi_s} + \lambda_{\psi_a}L_{\psi_a} + \lambda_{charge}L_{charge} \quad (22)$$

where λ terms are weighting hyperparameters.

3.6 Rayleigh damping coefficients

In order to minimize L_{total}, the coefficients α_R and β_R are considered as trainable parameters: α_R, β_R←are learnt by gradient descent

3.7 Implementation steps

Furthermore, the dimensionless parameters may be expressed as follows:

1. Describe the designs of neural networks for every field variable.
2. Examples of collocation points in the space $(\mathbb{x}_1, \theta_1, t)$.
3. Use automated differentiation to calculate derivatives.
4. Create loss terms for control relations, PDEs, BCs, and ICs.
5. Use a gradient-based optimizer to train the NNs by minimizing L_{total}.

Additionally, the dimensionless parameters may be written like this:

$$\overline{\Omega} = \Omega\sqrt{\frac{\rho_m}{E_m}}. \quad (23)$$

4. Results and discussion

The structure and material properties of the graphene oxide powders under discussion are shown in Ref. (Vu and Tran 2025).

4.1 Validation

Table 1 presents a validation study comparing the natural frequencies of a simply supported functionally graded cylindrical shell reinforced with graphene oxide powders, as predicted by the present formulation, against benchmark results reported by Loy *et al.* (Loy, Lam, and Reddy, 1999). The comparison is carried out for two gradient indices ($N = 0.5$ and $N = 30$) and for several circumferential mode numbers ($n = 1$ to 5) with axial mode $m = 1$. Across all cases, the present results exhibit excellent agreement with published data, with discrepancies consistently within a narrow margin, thereby confirming the accuracy of the higher-order shear deformation theory combined with the Halpin–Tsai micromechanical model. The influence of increasing gradient index is also evident, leading to a general reduction in natural frequencies, which reflects the enhanced metallic character and reduced stiffness of the graded structure. This validation underscores the robustness of the proposed PINN-based framework for reliable vibration analysis.

4.2 Parametric results

Fig. 4 illustrates the influence of boundary conditions on the dimensionless natural frequency $\overline{\Omega}_{11}$ of graphene oxide powder (GOP) reinforced tennis handles under varying temperature rise ΔT. Three support configurations—clamped–clamped, simply–simply, and clamped–simply—are considered to capture the structural constraints' role on vibrational stability. Results demonstrate a pronounced frequency reduction with increasing thermal load across all cases, highlighting the detrimental effect of temperature-induced softening. The clamped–clamped configuration maintains the highest natural frequency due to its superior constraint on transverse displacements and rotations, thereby enhancing stiffness. The simply–simply condition produces intermediate performance, while the clamped–simply case exhibits the lowest frequency response, reflecting its weaker restraining capability. As ΔT approaches approximately $70-80°C$, frequency collapse occurs, indicating the onset of thermoelastic instability. This comparison underscores the necessity of carefully designing support conditions for thermomechanically stable performance of nanocomposite-reinforced tennis handles. The PINN-enhanced framework effectively captures the nonlinear coupling between thermal effects, boundary conditions, and vibrational behavior,

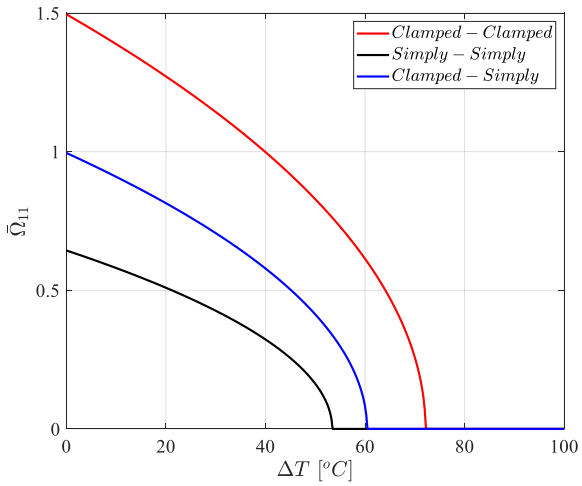

Fig. 4. The influence of boundary conditions on the dimensionless natural frequency $\bar{\boldsymbol{\Omega}}_{\mathbf{11}}$ of graphene oxide powder (GOP) reinforced tennis handles under varying temperature rise

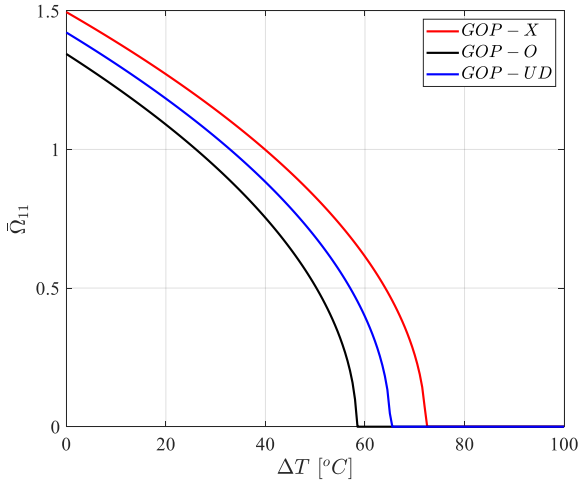

Fig. 5 The role of graphene oxide powder distribution patterns on the thermal-vibrational performance of nano-composite-reinforced tennis handles

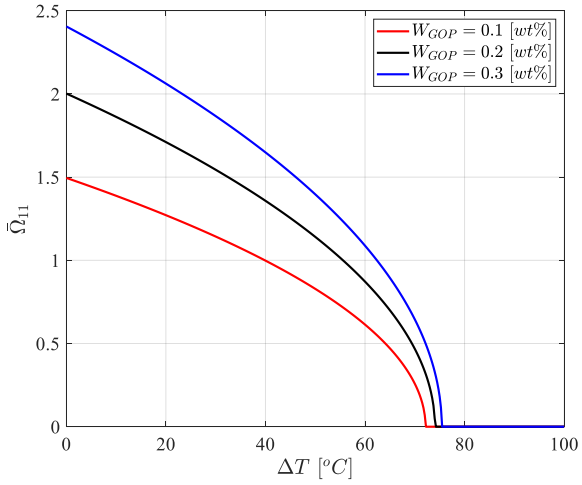

Fig. 6 The influence of graphene oxide powder weight fraction $\boldsymbol{W_{GOP}}$ on the dimensionless natural frequency $\bar{\boldsymbol{\Omega}}_{\mathbf{11}}$ of tennis handles under varying thermal environments

demonstrating predictive reliability beyond conventional methods. These results highlight how integrating optimized support design with graphene oxide reinforcement can strategically suppress instability, thereby improving the stiffness and durability of high-performance sports equipment.

Fig. 5 examines the role of graphene oxide powder (GOP) distribution patterns—namely GOP–X, GOP–O, and GOP–UD—on the thermal-vibrational performance of nanocomposite-reinforced tennis handles. The variation of the dimensionless natural frequency $\bar{\Omega}_{11}$ with increasing temperature change ΔT is presented, capturing the reinforcing efficiency of nonuniform filler dispersions. The GOP–X configuration exhibits the highest frequency response, reflecting its optimal reinforcement alignment in critical load-bearing directions, which enhances stiffness and suppresses shear deformations. The GOP–O pattern delivers an intermediate response, attributed to balanced reinforcement across orientations, while the GOP–UD (uniform distribution) case shows the lowest stiffness gain, indicating limited reinforcement effectiveness under thermal stresses. Across all distributions, increasing ΔT induces a monotonic frequency decline, ultimately leading to structural instability near $70-80°C$, marking the thermal buckling threshold. These findings highlight the critical role of filler distribution in tailoring vibration resistance and thermal stability of sports equipment. The results validate that optimized graphene oxide dispersion strategies can significantly elevate dynamic durability, ensuring superior performance under operational thermal fluctuations. By embedding these physical insights into the PINN framework, predictive accuracy is further enhanced, offering a robust pathway to intelligent design optimization for advanced tennis handle manufacturing.

Fig. 6 illustrates the influence of graphene oxide powder weight fraction W_{GOP} on the dimensionless natural frequency $\bar{\Omega}_{11}$ of tennis handles under varying thermal environments. Curves are presented for three reinforcement levels—$0.1\%, 0.2\%$, and 0.3%—capturing the progressive enhancement in structural rigidity with increased nanofiller incorporation. The results clearly reveal that higher W_{GOP} substantially elevates the natural frequency at lower ΔT, reflecting the stiffening effect imparted by the Halpin–Tsai-derived reinforcement mechanism. Specifically, the 0.3% configuration shows the most pronounced improvement, effectively resisting thermally induced frequency degradation and delaying the onset of instability to higher temperatures. Conversely, the 0.1% case demonstrates limited reinforcement, with frequencies rapidly declining as ΔT increases. The intermediate 0.2% loading provides a balanced performance between stiffness gain and reinforcement cost-efficiency. All curves converge toward instability beyond $70-80°C$, consistent with thermo-mechanical softening effects. This parametric evaluation emphasizes the importance of filler concentration in achieving optimal vibration suppression and thermal resilience. The PINN-based computational framework accurately predicts these nonlinear interactions, demonstrating its effectiveness in guiding nanocomposite material selection and reinforcement strategies for improved energy absorption and structural stability in sports applications.

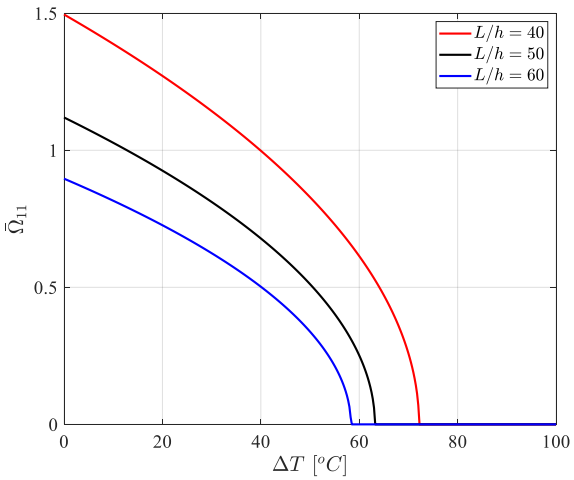

Fig. 7 The variation of the dimensionless natural frequency $\bar{\boldsymbol{\Omega}}_{\boldsymbol{11}}$ with respect to temperature change $\boldsymbol{\Delta T}$ for different slenderness ratios

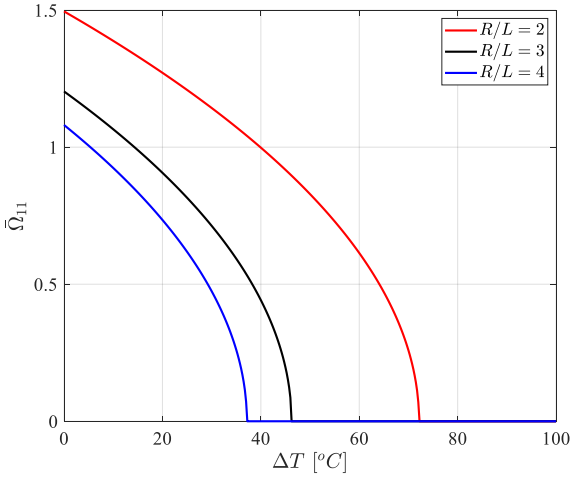

Fig. 8 The dependency of the dimensionless natural frequency $\bar{\boldsymbol{\Omega}}_{\boldsymbol{11}}$ on the temperature rise $\boldsymbol{\Delta T}$ for different geometric configurations characterized by radius-to-length ratios

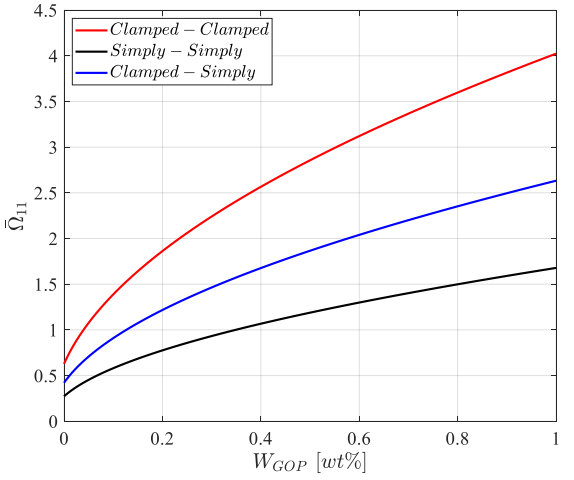

Fig. 9 The effect of graphene oxide powder (GOP) weight fraction $\boldsymbol{W_{GOP}}$ on the dimensionless natural frequency $\bar{\boldsymbol{\Omega}}_{\boldsymbol{11}}$, under three boundary conditions—clamped–clamped, simply–simply, and clamped–simply

Fig. 7 presents the variation of the dimensionless natural frequency $\bar{\Omega}_{11}$ with respect to temperature change ΔT for different slenderness ratios $L/h = 40,50,60$, providing insights into the geometric dependency of reinforced tennis handles. At lower ΔT, the shortest structure $(L/h = 40)$ demonstrates the highest frequency response due to its enhanced flexural rigidity and reduced susceptibility to bending deformations. As the slenderness increases to 50 and 60, the frequency gradually decreases, reflecting the softening effect of increased aspect ratios and reduced load-carrying stiffness. Across all configurations, temperature rise induces a nonlinear reduction in frequency, culminating in instability when approaching $70–80°C$, where the thermoelastic limit is reached. The results establish a clear trend that more slender structures are inherently less stable under thermal environments, emphasizing the necessity of geometric optimization alongside material reinforcement. The PINN framework, enriched with Legendre polynomial approximations, efficiently captures this geometric–thermal–vibrational coupling, providing accurate and computationally efficient predictions. These findings underline that careful control of slenderness ratio, combined with graphene oxide reinforcement strategies, is essential for designing thermomechanically reliable and vibration-resistant tennis handles in high-performance sports engineering applications.

Fig. 8 illustrates the dependency of the dimensionless natural frequency $\bar{\Omega}_{11}$ on the temperature rise ΔT for different geometric configurations characterized by radius-to-length ratios $R/L = 2,3,4$. Results indicate that as ΔT increases, all configurations exhibit a gradual decline in natural frequency, highlighting the destabilizing influence of thermal softening. Structures with smaller ratios $(R/L = 2)$ achieve higher baseline frequencies, reflecting superior geometric stiffness and resistance against bending deformation. Conversely, increasing R/L diminishes flexural rigidity, producing lower frequency responses and accelerated instability under elevated thermal fields. The onset of thermoelastic instability is consistently observed around $70–80°C$, although structures with larger R/L values reach instability earlier, confirming their vulnerability to heat-induced performance degradation. These observations emphasize the strong role of geometric design in determining the thermomechanical robustness of nanocomposite-reinforced tennis handles. Incorporation of the Halpin–Tsai model within the PINN framework enables accurate prediction of this nonlinear interaction, capturing the simultaneous influence of reinforcement efficiency, geometry, and temperature rise. The results suggest that optimizing radius-to-length ratio is an essential strategy, where lower R/L values are beneficial for maximizing stiffness, delaying instability onset, and ensuring reliable thermal-vibrational stability in advanced sports equipment design.

Fig. 9 presents the effect of graphene oxide powder (GOP) weight fraction W_{GOP} on the dimensionless natural frequency $\bar{\Omega}_{11}$, under three boundary conditions—clamped–clamped, simply–simply, and clamped–simply. Results reveal a nonlinear frequency enhancement with increasing W_{GOP}, reflecting the reinforcement efficiency of nanofillers

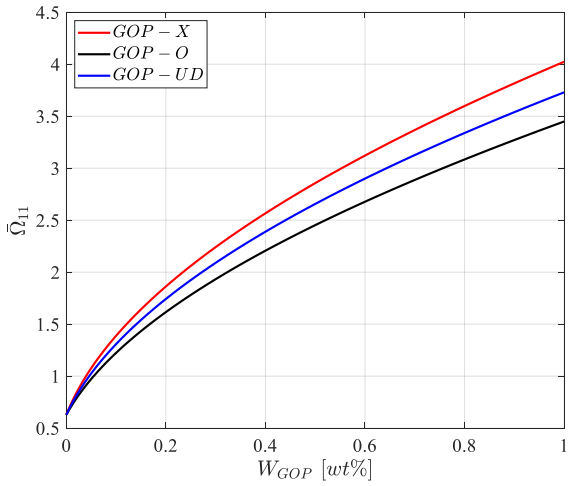

Fig. 10 The influence of graphene oxide powder distribution patterns on the variation of natural frequency $\bar{\Omega}_{11}$ with respect to W_{GOP}

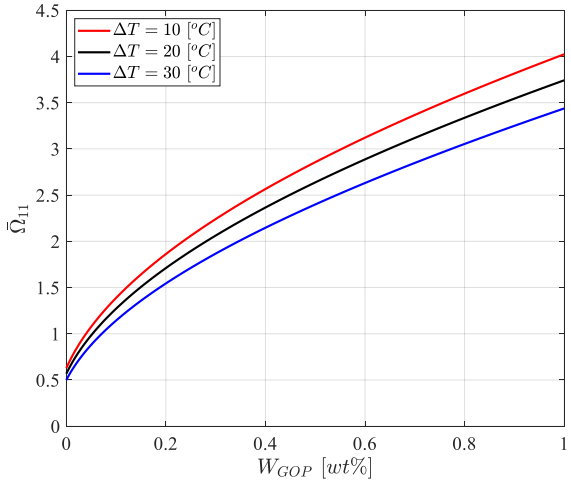

Fig. 11 The combined effect of temperature change ΔT and graphene oxide powder weight fraction W_{GOP} on the dimensionless natural frequency

as predicted by the Halpin–Tsai micromechanical model. The clamped–clamped configuration consistently yields the highest natural frequency due to its superior constraint, which minimizes displacement and rotation across the structure. The clamped–simply case shows intermediate gains, while the simply–simply condition demonstrates the lowest stiffness improvement. Notably, even small increments in W_{GOP} significantly elevate frequencies, highlighting the effectiveness of GOP inclusion in enhancing vibration resistance. However, the rate of improvement diminishes at higher concentrations, suggesting a saturation effect in reinforcement efficiency. These results underline that combined boundary optimization and nanofiller incorporation provide a dual mechanism for tailoring the thermomechanical performance of tennis handles. The physics-informed neural network framework ensures accurate prediction of these nonlinear reinforcement trends, while also enabling computationally efficient parametric explorations. Overall, the findings demonstrate that clamped–clamped supported tennis handles with elevated GOP fractions achieve superior vibrational stability, making them an ideal candidate for high-performance sports engineering applications requiring durability under dynamic loads.

Fig. 10 explores the influence of graphene oxide powder (GOP) distribution patterns—X, O, and uniformly distributed (UD)—on the variation of natural frequency $\bar{\Omega}_{11}$ with respect to W_{GOP}. The results reveal that all distributions produce a nonlinear enhancement in natural frequency as W_{GOP} increases, reflecting the reinforcing contribution of nanofillers. The GOP–X distribution consistently demonstrates the highest frequency response, owing to its alignment along critical load-bearing directions, which maximizes stiffness gain. The GOP–O pattern achieves intermediate performance by offering a balanced but less targeted reinforcement effect, whereas the GOP–UD distribution shows the lowest improvement, highlighting the inefficiency of uniform dispersion under vibrational loading. At higher filler fractions, the performance gap between distribution patterns becomes more pronounced, emphasizing the role of anisotropic reinforcement strategies in maximizing efficiency. The findings confirm that optimal nanofiller orientation is as significant as weight fraction in determining thermomechanical performance. By embedding these anisotropic reinforcement effects into the PINN framework enriched with Legendre polynomials, the model successfully captures complex distribution–frequency interactions. This provides designers with predictive insights into how tailored nanofiller distributions can enhance vibration control, ensuring durable and high-performing tennis handles for advanced sporting applications.

Fig. 11 investigates the combined effect of temperature change ΔT and graphene oxide powder weight fraction W_{GOP} on the dimensionless natural frequency $\bar{\Omega}_{11}$. Results are shown for $\Delta T = 10, 20,$ and 30°C. Across all cases, increasing W_{GOP} substantially elevates natural frequency, confirming the stiffening influence of nanofillers. However, rising thermal loads systematically reduce frequency, shifting the response curves downward. For example, at a given reinforcement level, the structure under $\Delta T = 30°C$ displays the lowest frequency, while $\Delta T = 10°C$ maintains the highest performance. This trend highlights the competition between thermally induced softening and nanofiller-driven stiffening, with reinforcement partially mitigating the adverse effects of elevated temperature. Importantly, the rate of frequency enhancement with W_{GOP} is maintained across different ΔT, suggesting that filler incorporation remains an effective design strategy even under moderate heating. The PINN approach, constrained by thermomechanical principles, accurately captures this coupled nonlinear interaction while providing efficient surrogate modeling capabilities. These findings suggest that careful balance between reinforcement concentration and expected operational temperature is critical for ensuring vibration stability and durability of graphene-reinforced tennis handles in practical applications.

Fig. 12 illustrates the variation of the dimensionless natural frequency $\bar{\Omega}_{11}$ of the tennis handle modeled as a nanocomposite-reinforced cylindrical shell, with respect to the graphene oxide powder weight fraction. The results are

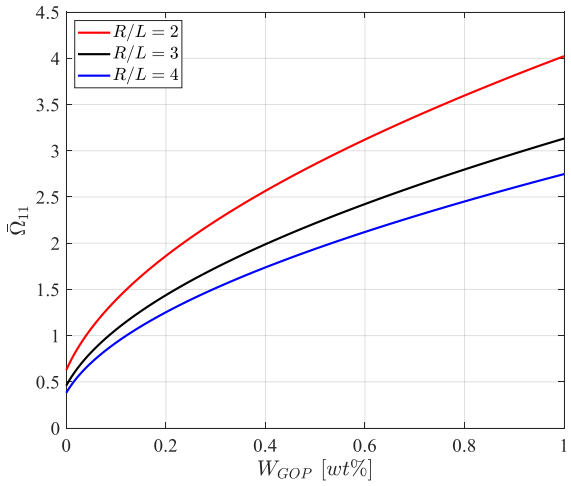

Fig. 12 The variation of the dimensionless natural frequency of the tennis handle modeled as a nanocomposite-reinforced cylindrical shell, with respect to the graphene oxide powder weight fraction

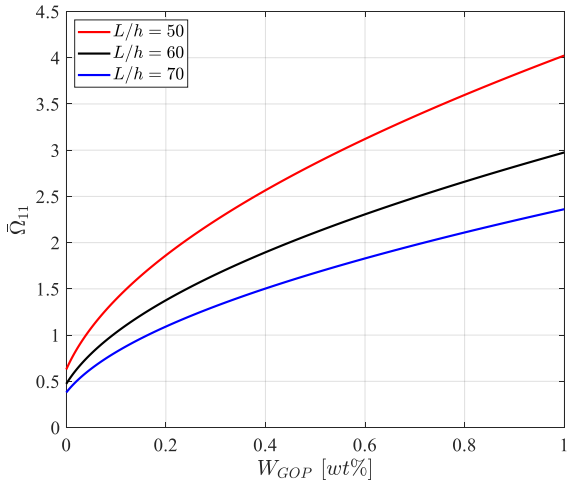

Fig. 13 The influence of aspect ratio on the variation of dimensionless natural frequency against graphene oxide powder weight fraction

presented for different radius-to-length ratios ($R/L = 2, 3, 4$), revealing a clear sensitivity of vibrational behavior to both geometric configuration and material reinforcement. As W_{GOP} increases, $\bar{\Omega}_{11}$ exhibits a monotonic growth, confirming the stiffening effect induced by graphene oxide inclusions through enhanced load transfer within the matrix, as captured by the Halpin–Tsai model. Among the cases, the structure with a smaller radius-to-length ratio ($R/L = 2$) consistently demonstrates the highest frequency values, indicating superior rigidity and resistance to dynamic deformation. In contrast, increasing the ratio (R/L=4) reduces the natural frequency, highlighting the impact of slenderness on structural flexibility. Overall, the figure establishes the reinforcing efficiency of GOP and the geometric dependency of vibrational characteristics.

Fig. 13 depicts the influence of aspect ratio on the variation of dimensionless natural frequency against graphene oxide powder weight fraction. Results are provided for $L/h = 50,60,70$, where L denotes the handle length and h the shell thickness. The findings indicate that for all configurations, increasing W_{GOP} enhances $\bar{\Omega}_{11}$, demonstrating that reinforcement through graphene oxide inclusion leads to higher structural stiffness and improved vibration resistance. However, the role of slenderness is evident: at lower $L/h = 50$, the natural frequency attains its maximum, reflecting higher stiffness associated with thicker geometries. Conversely, larger L/h values, corresponding to thinner shells, reduce $\bar{\Omega}_{11}$, signifying increased flexibility and susceptibility to vibrational excitation. The nonlinear growth trend with respect to W_{GOP} reflects the synergy between micromechanical reinforcement and geometric parameters. This figure emphasizes the balance between nanocomposite reinforcement and aspect ratio in optimizing tennis handle dynamics.

5. Conclusions

In this study, a comprehensive framework for improving tennis handle performance has been proposed by integrating graphene oxide powder nanocomposites with advanced modeling techniques and physics-informed deep neural networks. The tennis handle has been modeled as a cylindrical shell structure, which has allowed for an accurate representation of its mechanical and vibrational responses under sports-related dynamic conditions. The Halpin–Tsai model has been successfully employed to predict the effective elastic properties of the graphene oxide–reinforced polymer, and it has provided reliable estimations of stiffness improvements due to nanoscale reinforcements. Furthermore, a Taylor series expansion-based higher-order shear deformation theory has been formulated, which has captured transverse shear deformation effects with greater accuracy than lower-order theories. The governing dynamic equations have been systematically derived using Hamilton's principle, ensuring energy consistency and mathematical rigor in describing the system's behavior. To solve these complex equations efficiently, a PINN architecture enriched with Legendre polynomial expansions has been introduced. This approach has enabled the incorporation of physical constraints into the learning process while also improving approximation smoothness and accuracy. By combining the physics-based formulation with data-driven learning, the method has achieved high accuracy with reduced computational effort when compared to conventional numerical methods. Results have shown that graphene oxide nanocomposites have significantly enhanced the stiffness, damping capacity, and vibration suppression characteristics of tennis handles. The PINN-based solutions have demonstrated excellent agreement with benchmark models, confirming the robustness and efficiency of the proposed methodology. Through this integration of nanomaterial engineering and AI-based computational mechanics, the study has provided a pathway toward designing optimized tennis handles with superior durability, comfort, and energy absorption. Overall, the research has demonstrated that physics-informed deep

learning approaches can be successfully applied to sports engineering problems. By bridging material science, structural mechanics, and artificial intelligence, the proposed framework has offered valuable contributions to both theoretical development and practical applications. This work has also opened opportunities for extending the methodology to other sports equipment and to broader engineering applications where nanocomposite materials and PINNs have played a transformative role in performance optimization.

Acknowledgement

This study was supported by the National Social Science Foundation Project: Study on the Formation Mechanism, Current Situation Evaluation and Realization Path of Low-carbon Development and Utilization of Outdoor Sports Resources in China (No. 24BTY064).

References

Al-Houri, S., Al-Osta, M.A., Gawah, Q., Bourada, F., Tounsi, A., Al-Dulaijan, S.U. and Tounsi, A. (2024), "Wave propagation analysis of composite beams reinforced with nonlinear fg-cnt distributions supported on kerr elastic foundation utilizing an improved integral first-order shear deformation theory", *Geomech. Eng.*, **39**(5), 483. https://doi.org/10.12989/gae.2024.39.5.483

Avcar, M., Hadji, L. and Civalek, O. (2023), "The influence of non-linear carbon nanotube reinforcement on the natural frequencies of composite beams", *Adv. Nano Res.*, **14**(5), 421-433. https://doi.org/10.12989/anr.2023.14.5.421

Azmi, M., Kolahchi, R. and Bidgoli, M.R. (2019), "Dynamic analysis of concrete column reinforced with sio2 nanoparticles subjected to blast load", *Adv. Concr. Constr.*, **7**(1), 51. https://doi.org/10.12989/acc.2019.7.1.051

Beitollahi, A., Janghorban, M., Bazargan-Lari, Y. and Tounsi, A. (2025), "On the variable length scale parameter for agglomeration of nanoparticles in nanocomposites", *Proceedings of the Institution of Mechanical Engineers, Part C: Journal of Mechanical Engineering Science*, 09544062241308513. https://doi.org/10.1177/09544062241308513

Belabed, Z., Bousahla, A.A. and Tounsi, A. (2024), "Vibrational and elastic stability responses of functionally graded carbon nanotube reinforced nanocomposite beams via a new quasi-3d finite element model", *Comput. Concr.*, **34**(5), 625-648. https://doi.org/10.12989/cac.2024.34.5.625

Belabed, Z., Tounsi, A., Bousahla, A.A., Tounsi, A., Khedher, K. M. and Salem, M.A. (2024), "Mechanical behavior analysis of fg-cntrc porous beams resting on winkler and pasternak elastic foundations: a finite element approach", *Comput. Concr.*, **34**(4), 447-476. https://doi.org/10.12989/cac.2024.34.4.447

Bentrar, H., Chorfi, S.M., Belalia, S.A., Tounsi, A., Ghazwani, M.H. and Alnujaie, A. (2023), "Effect of porosity distribution on free vibration of functionally graded sandwich plate using the p-version of the finite element method", *Struct. Eng. Mech.*, **88**(6), 551-567. https://doi.org/10.12989/sem.2023.88.6.551

Djebbour, K.D., Nebab, M., Avcar, M., Ait Atmane, H., Bernard, F., Bennai, R. and Ikinci, B. (2025), "Stability and vibration analysis of shear deformable fg-cntrc beams resting on elastic foundations", *Adv. Nano Res.*, **18**(3), 205-221. https://doi.org/10.12989/anr.2025.18.3.205

Ebrahimi, F. and Salari, E. (2018), "Effect of non-uniform temperature distributions on nonlocal vibration and buckling of inhomogeneous size-dependent beams", *Adv. Nano Res.*, **6**(4), 377. https://doi.org/10.12989/anr.2018.6.4.377

Ebrahimi, F., Dehghan, M. and Seyfi, A. (2019), "Eringen's nonlocal elasticity theory for wave propagation analysis of magneto-electro-elastic nanotubes", *Adv. Nano Res.*, **7**(1), 1. https://doi.org/10.12989/anr.2019.7.1.001

Ebrahimi, F., Dehghan, M. and Seyfi, A. (2019), "Eringen's nonlocal elasticity theory for wave propagation analysis of magneto-electro-elastic nanotubes", *Adv. Nano Res.*, **7**(1), 1. https://doi.org/10.12989/anr.2019.7.1.001

Ehyaei, J., Ebrahimi, F. and Salari, E. (2016), "Nonlocal vibration analysis of fg nano beams with different boundary conditions", *Adv. Nano Res.*, **4**(2), 085. https://doi.org/10.12989/anr.2016.4.2.085

Garg, A.K., Khare, R.K. and Kant, T. (2006), "Higher-order closed-form solutions for free vibration of laminated composite and sandwich shells", *J. Sandw. Struct. Mater.*, **8**(2), 95-124. https://doi.org/10.1177/1099636206058688

Gawah, Q., Bourada, F., Al-Osta, M.A., Tahir, S.I., Tounsi, A. and Yaylacı, M. (2024), "An improved first-order shear deformation theory for wave propagation analysis in fg-cntrc beams resting on a viscoelastic substrate", *Int. J. Struct. Stabil. Dyn.*, **25**(1), 2550010. https://doi.org/10.1142/S0219455425500105

Gawah, Q., Al-Osta, M.A., Bourada, F., Tounsi, A., Ahmad, S. and Al-Zahrani, M.M. (2025), "Bending analysis of graphene platelet-reinforced FG plates on kerr foundations using an integral HSDT", *Acta Mechanica*, 1-25. https://doi.org/10.1007/s00707-025-03877-5

Hajmohammad, M.H., Zarei, M.S., Farrokhian, A. and Kolahchi, R. (2018), "A layerwise theory for buckling analysis of truncated conical shells reinforced by cnts and carbon fibers integrated with piezoelectric layers in hygrothermal environment", *Adv. Nano Res.*, **6**(4), 299. https://doi.org/10.12989/anr.2018.6.4.299

Jayakumari, B.Y., Swaminathan, E.N. and Partheeban, P. (2024), "Sustainable construction material using nanosilica and multi-walled carbon nanotubes in cement concrete", *Adv. Nano Res.*, **16**(5), 459-472. https://doi.org/10.12989/anr.2024.16.5.459

Kadiri, A., Bendaida, M., Attia, A., Balubaid, M., Mahmoud, S., Bousahla, A.A., Tounsi, A., Bourada, F. and Tounsi, A. (2024), "Wave propagation in fg polymer composite nanoplates embedded in variable elastic medium", *Adv. Nano Res.*, **17**(3), 235-248. https://doi.org/10.12989/anr.2024.17.3.235

Liu, T., Wang, A., Wang, Q., Qin, B. and Xie, F. (2021), "Chebyshev formulation for in-plane vibration analysis of arbitrary laminated polygonal plates", *AIAA J.*, **59**(7), 2753-2767. https://doi.org/10.2514/1.J060121

Loy, C., Lam, K. and Reddy, J. (1999), "Vibration of functionally graded cylindrical shells", *Int. J. Mech. Sci.*, **41**(3), 309-324. https://doi.org/10.1016/S0020-7403(98)00054-X

Madenci, E., Ozkilic, Y.O., Hakamy, A. and Tounsi, A. (2023), "Experimental tensile test and micro-mechanic investigation on carbon nanotube reinforced carbon fiber composite beams", *Adv. Nano Res.*, **14**(5), 443-450. https://doi.org/10.12989/anr.2023.14.5.443

Moradi, H., Atashi, P., Amelirad, O., Yang, J.K., Chang, Y.Y. and Kamranifard, T. (2022), "Machine learning modeling and doe-assisted optimization in synthesis of nanosilica particles via stöber method", *Adv. Nano Res.*, **12**(4), 387. https://doi.org/10.12989/anr.2022.12.4.387

Sadd, M.H. (2009), *Elasticity: Theory, Applications, and Numerics*, Academic Press. https://doi.org/10.1016/B978-0-12-374446-3.X0001-3

Safarpour, M., Rahimi, A., Alibeigloo, A., Bisheh, H. and Forooghi, A. (2021), "Parametric study of three-dimensional bending and frequency of fg-gplrc porous circular and annular

plates on different boundary conditions", *Mech. Based Des. Struct.*, **49**(5), 707-737. https://doi.org/10.1080/15397734.2020.1719509

Salari, E., Ashoori, A. and Vanini, S.A.S. (2019), "Porosity-dependent asymmetric thermal buckling of inhomogeneous annular nanoplates resting on elastic substrate", *Adv. Nano Res.*, **7**(1), 25. https://doi.org/10.12989/anr.2019.7.1.025

Shen, X., Li, T., Xu, L., Kiarasi, F., Babaei, M. and Asemi, K. (2024), "Free vibration analysis of fg porous spherical cap reinforced by graphene platelet resting on winkler foundation", *Adv. Nano Res.*, **16**(1), 11-26. https://doi.org/10.12989/anr.2024.16.1.011

Tounsi, A., Belabed, Z., Bounouara, F., Balubaid, M., Mahmoud, S., Bousahla, A.A. and Tounsi, A. (2024), "A finite element approach for forced dynamical responses of porous FG nanocomposite beams resting on viscoelastic foundations", *Int. J. Struct. Stabil. Dyn.*, 2650078. https://doi.org/10.1142/S021945542650078X

Vu, V.T. and Tran, H.Q. (2025), "Thermo-electro-magneto-mechanical vibration analysis of sandwich plates with graphene oxide powder reinforced composite core and magneto-electro-elastic face sheets resting on Kerr foundation", *Int. J. Mech. Mater. Des.*, 1-33. https://doi.org/10.1007/s10999-025-09795-z

Xia, L., Wang, R., Chen, G., Asemi, K. and Tounsi, A. (2023), "The finite element method for dynamics of fg porous truncated conical panels reinforced with graphene platelets based on the 3-d elasticity", *Adv. Nano Res.*, **14**(4), 375-389. https://doi.org/10.12989/anr.2023.14.4.375

Ye, W., Shi, Y., Zhou, Q., Xie, M., Wang, H., Bou-Saïd, B. and Liu, W. (2024), "Recent advances in self-lubricating metal matrix nanocomposites reinforced by carbonous materials: A review", *Nano Mater. Sci.*, **6**(6), 701-713. https://doi.org/10.1016/j.nanoms.2024.04.002

Youzera, H., Meftah, S. A., Tounsi, A., Salem, M. A., Khedher, K. M. and Yaylacı, M. (2025), "Free vibration analysis of sandwich cylindrical shells with functionally graded carbon nanotube-reinforced composite face sheets using the differential quadrature (dq) method", *Acta Mechanica*, 1-16. https://doi.org/10.1007/s00707-025-03876-6

Zerrouki, R., Karas, A. and Zidour, M. (2020), "Critical buckling analyses of nonlinear fg-cnt reinforced nano-composite beam", *Adv. Nano Res.*, **9**(3), 211-220. https://doi.org/10.12989/anr.2020.9.3.211

Zhao, T., Chen, Y., Ma, X., Linghu, S. and Zhang, G. (2022), "Free transverse vibration analysis of general polygonal plate with elastically restrained inclined edges", *J. Sound Vib.*, **536**, 117151. https://doi.org/10.1016/j.jsv.2022.117151

CC